Title
Characterization of a Nitrogenase Iron Protein Substituted with a Synthetic [Fe_4 Se_4] Cluster.

Journal
Angewandte Chemie (International ed. in English), 61(19)

ISSN
1433-7851

Authors
Solomon, Joseph B
Tanifuji, Kazuki
Lee, Chi Chung
et al.

Publication Date
2022-05-01

DOI
10.1002/anie.202202271

Peer reviewed

HHS Public Access
Author manuscript
Angew Chem Int Ed Engl. Author manuscript; available in PMC 2023 May 02.

Published in final edited form as:
Angew Chem Int Ed Engl. 2022 May 02; 61(19): e202202271. doi:10.1002/anie.202202271.

Characterization of a Nitrogenase Iron Protein Substituted with a Synthetic [Fe_4Se_4] Cluster

Joseph B. Solomon[+,a,b], **Kazuki Tanifuji**[+,a,c], **Chi Chung Lee**[a], **Andrew J. Jasniewski**[a], **Britt Hedman**[d], **Keith O. Hodgson**[d,e], **Yilin Hu**[a], **Markus W. Ribbe**[a,b]

[a]Department of Molecular Biology and Biochemistry, University of Califronia, Irvine, Irvine, CA 92697-3900 (USA)

[b]Department of Chemistry, University of California, Irvine, Irvine, CA 92697-2025 (USA)

[c]Institute for Chemical Research, Kyoto University, Gokasho, Uji, Kyoto 611-0011 (Japan)

[d]Stanford Synchrotron Radiation Lightsource, SLAC National Accelerator Laboratory, Stanford University, Menlo Park, CA 94025 (USA)

[e]Department of Chemistry, Stanford University, Stanford, CA 94305 (USA)

Abstract

The Fe protein of nitrogenase plays multiple roles in substrate reduction and cluster maturation via its redox active [Fe_4S_4] cluster. Here we report the synthesis and characterization of a water-soluble [Fe_4Se_4] cluster that is used to substitute the [Fe_4S_4] cluster of the *Azotobacter vinelandii* Fe protein (*Av*NifH). Biochemical, EPR and XAS/EXAFS analyses demonstrate the ability of the [Fe_4Se_4] cluster to adopt the super-reduced, all-ferrous state upon its incorporation into *Av*NifH. Moreover, these studies reveal that the [Fe_4Se_4] cluster in *Av*NifH already assumes a partial all-ferrous state ($[Fe_4Se_4]^0$) in the presence of dithionite, where its [Fe_4S_4] counterpart in *Av*NifH exists solely in the reduced state ($[Fe_4S_4]^{1+}$). Such a discrepancy in the redox properties of the *Av*NifH-associated [Fe_4Se_4] and [Fe_4S_4] clusters can be used to distinguish the differential redox requirements for the substrate reduction and cluster maturation of nitrogenase, pointing to the utility of chalcogen-substituted FeS clusters in future mechanistic studies of nitrogenase catalysis and assembly.

Graphical Abstract

yilinh@uci.edu, mribbe@uci.edu.
[+]These authors contributed equally.

Supporting information for this article is given via a link at the end of the document.

This work is dedicated to Prof. Richard H. Holm.

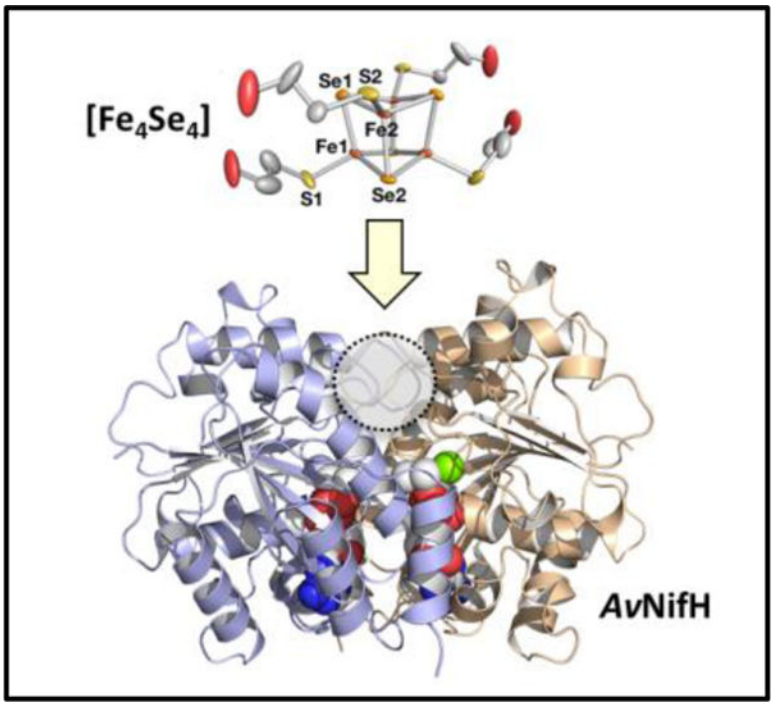

A synthetic $[Fe_4Se_4]$ compound is incorporated into the nitrogenase iron protein, showing redox properties distinct from its $[Fe_4S_4]$ counterpart that can be used to distinguish the differential redox requirements of nitrogenase catalysis and assembly.

Keywords

nitrogenase; iron protein; $[Fe_4Se_4]$ cluster; catalysis; biosynthesis

Introduction

The nitrogenase Fe protein plays a key role in the activation and reduction of a variety of small-molecule substrates, including N_2, CO_2, CO and C_2H_2, under ambient conditions. Designated *Av*NifH, the Fe protein of the Mo-nitrogenase from *Azotobacter vinelandii* is a homodimer of ~60 kDa that contains a subunit-bridging $[Fe_4S_4]$ cluster and an MgATP-binding site in each subunit.[1–5] *Av*NifH carries out its function in catalysis by serving as an electron donor for its catalytic partner, MoFe protein (designated *Av*NifDK), within the nitrogenase complex (Figure S1a);[6,7] alternatively, it can act as a reductase on its own to directly support substrate reduction (Figure S1b).[8–10] As an electron donor, *Av*NifH transfers electrons concomitantly with ATP hydrolysis from its $[Fe_4S_4]$ cluster, via the P-cluster ($[Fe_8S_7]$), to the M-cluster (or the cofactor; [(*R*-homocitrate)$MoFe_7S_9C$]) of *Av*NifDK, where reduction of substrates, such as N_2, H^+, CO and C_2H_2, takes place (Figure S1a).[1–7,11–13] As an independent reductase, *Av*NifH converts CO_2 to CO at its $[Fe_4S_4]$ cluster under both *in vivo* and *in vitro* conditions, and this reaction can occur in the presence or absence of ATP (Figure S1b).[8–10] Other than playing a crucial role in catalysis, *Av*NifH is also indispensable for the biosynthesis of the P- and M-clusters of its catalytic partner,

*Av*NifDK. In the case of the former, *Av*NifH couples a [Fe_4S_4] cluster pair into a P-cluster at the α/β-subunit interface of *Av*NifDK (Figure S1c).[5,14,15] In the case of the latter, *Av*NifH inserts Mo and homocitrate into a [Fe_8S_9C] precursor on *Av*NifEN, a biosynthetic scaffold that shares a good degree of sequence and structural homology with *Av*NifDK, to yield a mature M-cluster that is subsequently transferred to the cofactor binding site within *Av*NifDK (Figure S1c).[5,14,15] In both cases, *Av*NifH likely uses a mode-of-action analogous to that in nitrogenase catalysis, functioning as an ATP-dependent reductase to facilitate the assembly of the complex metalloclusters of *Av*NifDK.[5,14,15]

The ability of the Fe protein to serve as a multifunctional reductase relies on the redox versatility of its [Fe_4S_4] center. It has been demonstrated that the [Fe_4S_4] cluster of *Av*NifH can undergo reversible redox changes among three oxidation states, namely, the oxidized ([Fe_4S_4]$^{2+}$), reduced ([Fe_4S_4]$^{1+}$), and super-reduced, all-ferrous ([Fe_4S_4]^{0}) states.]2,16] Under *in vivo* conditions, *Av*NifH is reduced by ferredoxin(s) or flavodoxin(s); whereas for *in vitro* assays, the physiological electron donors of *Av*NifH are replaced by suitable, artificial reductants.[2,4] The *in vitro* reduction of CO_2 can be achieved by *Av*NifH as an independent enzyme with or without MgATP in the presence of a strong reductant, Eu^{II}-DTPA ($E_{1/2}$ = −1.14 V at pH 8),[8–10,17] where the cluster of *Av*NifH adopts the super-reduced, all-ferrous [Fe_4S_4]^{0} state.[18] The *in vitro* reduction of substrates by the complete nitrogenase enzyme, on the other hand, is usually conducted in the presence of dithionite (*e.g.*, $E_{1/2}$ = −0.47 V at 2 mM dithionite, pH=8) and MgATP, where *Av*NifH is poised at the reduced, [Fe_4S_4]$^{1+}$ state and undergoes a reversible one-electron redox process to the oxidized, [Fe_4S_4]$^{2+}$ state to enable electron transfer to *Av*NifDK concomitant with ATP hydrolysis.[2] Binding of ATP lowers the midpoint potentials of the [Fe_4S_4] cluster of *Av*NifH from −290 mV to −430 mV[4] while inducing a conformational change of the protein, which in turn permits *Av*NifH to interact with its catalytic partner *Av*NifDK and facilitates the transfer of electrons from the former to the latter for substrate turnover.[1–7] Given the same requirement of dithionite and MgATP in assembly and catalysis, and the homologous interactions between *Av*NifH and its respective partners in these processes, the assembly of the P- and M-clusters on *Av*NifDK and *Av*NifEN, respectively, could involve mechanisms analogous to that employed in catalysis. However, there must be distinct reactivities of *Av*NifH in these processes—either in terms of its redox properties or related to its ability to interact with its partner protein—that allow this Fe protein to switch between the many roles it plays in substrate reduction and cluster assembly. Understanding how *Av*NifH functions in these processes is of crucial importance for the mechanistic investigation of nitrogenase. As such, it is necessary to develop a strategy that modifies the reactivities of *Av*NifH for the subsequent evaluation of its impact on nitrogenase catalysis and biosynthesis.

One effective way to alter the reactivity of the Fe protein is to replace the bridging sulfides in its [Fe_4S_4] cluster by selenides. In a previous study, NifS, a pyridoxal cysteine desulfurase,[19] was used along with selenocysteine and ferrous ammonium sulfate as the sources of Se and Fe for the *in vitro* reconstitution of apo NifH from *Klebsiella pneumoniae*. Subsequent chemical, EXAFS and kinetic analyses demonstrated small adjustments of the protein structure, yet apparent effects of Se substitution on substrate reduction, ATP hydrolysis, and the Fe protein cycle of nitrogenase.[20] In this study, we report the synthesis

and characterization of a water-soluble $[PPh_4]_2[Fe_4Se_4(SCH_2CH_2\ OH)_4]$ cluster that is used to reconstitute the apo NifH protein of *A. vinelandii*. Our biochemical, EPR and XAS/EXAFS analyses reveal that, contrary to its $[Fe_4S_4]$ counterpart, the $[Fe_4Se_4]$ cluster in *Av*NifH already exists in a partial all-ferrous state ($[Fe_4Se_4]^0$) in the presence of dithionite. Such a feature can be used to discern differential redox requirements for the substrate-reduction and cluster-maturation processes of nitrogenase, pointing to a potential utility of chalcogen-substituted Fe proteins in capturing catalytic and biosynthetic intermediates for future mechanistic studies of nitrogenase.

Results and Discussion

The water-soluble $[PPh_4]_2[Fe_4Se_4(SCH_2CH_2OH)_4]$ cluster was synthesized and characterized by x-ray crystallographic analysis (Tables S1–S3). The crystal structure of the $[PPh_4]_2[Fe_4Se_4(SCH_2CH_2OH)_4]$ cluster (designated $[Fe_4Se_4]^{Syn}$; Figure 1a),[21] like that of the previously synthesized $[PPh_4]_2[Fe_4S_4(SCH_2CH_2OH)_4]$ cluster (designated $[Fe_4S_4]^{Syn}$)[22] is consistent with a cuboidal $[Fe_4E_4]$ (E=S or Se) conformation. The overall structure of $[Fe_4Se_4]^{Syn}$ is similar to those of the previously reported, synthetic $[Fe_4Se_4]$ clusters bearing thiolate ligands, with each Fe atom binding three core Se atoms and a thiolate ligand in a distorted tetrahedral geometry. The mean Fe-Se, Fe-Fe, and Fe-S(thiolate) distances of $[Fe_4Se_4]^{Syn}$ are 2.41(4) Å, 2.78(4) Å, and 2.26 Å, respectively, showing no significant difference from other $[Fe_4Se_4(SR)_4]^{2-}$ compounds (R = Me, Et, or Ph),[23–26] as well as the one-electron-reduced $[Fe_4Se_4(SR)_4]^{3-}$ compounds (R = Et or Ph)[24,27,28] (Table S4). A superimposition of $[Fe_4Se_4]^{Syn}$ with $[Fe_4S_4]^{Syn}$ reveals a slightly expanded inorganic core of the Se-substituted cluster than its S-containing counterpart[29] (Figure 1b, c). This difference is ascribed to a larger Se_4 tetrahedron (6.74 $Å^3$) than a S_4 tetrahedron (5.52 $Å^3$) despite a similarity in the corresponding volumes of the Fe_4 tetrahedra in $[Fe_4Se_4]^{Syn}$ (2.52 $Å^3$) and $[Fe_4S_4]^{Syn}$ (2.38 $Å^3$). A parallel trend was also observed previously when the S atoms of the $[Fe_4S_4]$ cluster was replaced with Te.[30] The geometries of the Fe centers in $[Fe_4Se_4]^{Syn}$ and $[Fe_4S_4]^{Syn}$, on the other hand, do not show much difference, showing similar τ_4/τ_4' parameters[31,32] (0.96/0.93 for $[Fe_4Se_4]^{Syn}$ *vs.* 0.93/0.91 for $[Fe_4S_4]^{Syn}$) that are compatible with a tetrahedral geometry of a coordination center.

The Fe and Se K-edge XAS/EXAFS analyses of $[Fe_4Se_4]^{Syn}$ (Figure 2a–e; Tables S5–9) are in good agreement with the crystallographically derived structural metrics and the previously reported Se K-edge XAS analysis of the Fe/Se-reconstituted *Kp*NifH.[20] The areas under the pre-edge peaks of the Fe K-edge XAS spectra of $[Fe_4S_4]^{Syn}$ and $[Fe_4Se_4]^{Syn}$, originating from a dipole-forbidden 1s→3d transition that increases in intensity as the metal center is distorted away from centrosymmetry,[33,34] are 24.7 and 20.2 units (Table S5; Figure 2a), respectively. The Se K-edge EXAFS data provides further insights into the bonding characteristics of $[Fe_4Se_4]^{Syn}$. The best fit of the Se K-edge data (Table S6; Figure 2d, e) contains two Se–Fe scatterers at 2.41 Å, consistent with Se–Fe bonds in a cubane; additionally, there is a longer range Se---Fe interaction at 4.09 Å that corresponds to the cross-cubane distance. The Se---Se interactions are best fit with one scatterer at 3.82 Å, although a very similar fit with two such interactions results in a marginal increase in the goodness-of-fit parameter.

The successful synthesis of $[Fe_4Se_4]^{Syn}$ provides a useful tool for a 'clean' reconstitution of apo proteins without impurities often introduced by the traditional Fe/Se-based reconstitution methods. Using a protocol adapted from that previously reported for the reconstitution of apo *Av*NifH with $[Fe_4S_4]^{Syn}$, we reconstituted apo *Av*NifH with $[Fe_4Se_4]^{Syn}$ and compared the resulting protein (designated *Av*NifH^{Se}) with the native *Av*NifH in the oxidized (by IDS), reduced (by dithionite), and super-reduced (by Ti^{III} citrate or Eu^{II}-DTPA) states. The best fit of the Fe K-edge data (Figure 3a, b; Table S6) reveals that Fe–Se distances in the $[Fe_4Se_4]$ cluster of *Av*NifH^{Se} are between 2.41 Å and 2.45 Å, approximately 0.1 Å longer than the Fe–S distances observed in the $[Fe_4S_4]$ cluster of *Av*NifH (Figure 3c, d; Table S6). Similarly, the Fe---Fe distance of the $[Fe_4Se_4]$ cluster in *Av*NifH^{Se} is slightly longer than that of the $[Fe_4S_4]$ cluster in *Av*NifH, showing values of ~2.8 Å and ~2.7 Å, respectively (Table S6). What is most intriguing, however, is how the Fe K-edge energies and pre-edge areas in the spectra of the two cluster species in *Av*NifH and *Av*NifH^{Se} differ from each other upon redox transition (Figure 3e; Table S5). In the case of *Av*NifH, the K-edge energy decreases as the oxidation state of the $[Fe_4S_4]$ cluster decreases; specifically, there is a 0.4 eV shift in the K-edge from 7118.4 eV (oxidized state) to 7118.0 eV (reduced state) and another 0.8 eV shift to 7117.2 eV (super-reduced state) upon reduction of the $[Fe_4S_4]$ cluster in *Av*NifH (Figure 3e, *lower*, *brown circles*). In contrast, while there is a 1.0 eV decrease in the K-edge energy of *Av*NifH^{Se} from 7118.3 eV (oxidized state) to 7117.3 eV (reduced state), further reduction does not change the K-edge energy much and yields a very similar value of 7117.5 eV (super-reduced state) (Figure 3e, *upper*, *brown circles*). In addition, the areas of the pre-edge peaks in the spectra of *Av*NifH and *Av*NifH^{Se} show the same patterns of changes as those of their respective K-edge energies upon reduction. In the case of *Av*NifH, the pre-edge area decreases almost linearly with decreasing oxidation state, which indicates a distortion away from a tetrahedral symmetry around the Fe centers of the $[Fe_4S_4]$ cluster in this protein (Figure 3e, *lower*, *black circles*); whereas in the case of *Av*NifH^{Se}, the pre-edge area decreases upon transition from the oxidized state to the reduced state, yet it does not undergo further decrease upon transition to the super-reduced state (Figure 3e, *upper*, *black circles*).

Interestingly, the K-edge energy and pre-edge area of the reduced *Av*NifH^{Se} (Figure 3e, *upper*, Table S5) closely resemble those of the super-reduced *Av*NifH (Figure 3e, *upper*, Table S5), suggesting that the $[Fe_4Se_4]$ cluster in *Av*NifH^{Se} has already adopted, at least in part, the super-reduced, all-ferrous state at a more positive reduction potential generated by dithionite. To gather support for this argument, we performed comparative EPR analysis of *Av*NifH and *Av*NifH^{Se} in the presence of IDS, dithionite and Eu^{II}-DTPA (Figure 4). As expected, the IDS-oxidized *Av*NifH and *Av*NifH^{Se} are both EPR silent, consistent with the presence of diamagnetic $[Fe_4S_4]^{2+}$ and $[Fe_4Se_4]^{2+}$ clusters in these oxidized ('Ox') proteins (Figure 4a). Upon reduction with dithionite, both *Av*NifH and *Av*NifH^{Se} are present in a mixed $S = 1/2 : S = 3/2$ state that is associated with the $[Fe_4S_4]^{1+}$ and $[Fe_4Se_4]^{1+}$ clusters in these reduced ('Red') proteins (Figure 4a). However, compared to *Av*NifH, *Av*NifH^{Se} displays a slightly broader $S = 1/2$ signal at a substantially reduced intensity as well as a much more pronounced $S = 3/2$ signal, which is consistent with the previously reported EPR features of synthetic or protein-bound $[Fe_4Se_4]$ clusters.[24,35,36] As a further departure from its *Av*NifH counterpart, *Av*NifH^{Se} already demonstrates the $g = 16.4$ parallel-mode

signal that is characteristic of the all-ferrous $[Fe_4Se_4]^0$ cluster in the presence of dithionite, and this signal becomes more apparent in the presence of Eu^{II}-DTPA (Figure 4b). Such an all-ferrous state signal is absent from the spectrum of the dithionite-reduced *Av*NifH and only appears in the spectrum of the Eu^{II}-DTPA treated, super-reduced ('SR') *Av*NifH (Figure 4b). Taken together, the observation derived from EPR analysis is in good agreement with that derived from the Fe K-edge and pre-edge analyses, which collectively point to a mixed +1/0 oxidation state of the reduced $[Fe_4Se_4]$ cluster in *Av*NifH^{Se} at a solution potential where the $[Fe_4S_4]$ cluster in *Av*NifH exists solely in the +1 oxidation state.

The redox properties of *Av*NifH^{Se} and *Av*NifH were further probed by redox titration experiments, which revealed a midpoint potential of −240 mV and −285 mV, respectively, for the $[Fe_4Se_4]^{2+/'1+'}$ couple (in *Av*NifH^{Se}) and the $[Fe_4Se_4]^{2+/1+}$ couple (in *Av*NifH) (Figure 5a). The redox titration of the $[Fe_4Se_4]^{'1+'/0}$ couple, on the other hand, proved difficult in the absence of proper redox mediators. To circumvent this problem, we treated *Av*NifH and *Av*NifH^{Se} with 20 mM dithionite ($E_{1/2}$ = –0.44 V at pH 8.0), 2 mM dithionite ($E_{1/2}$ = –0.47 V at pH 8.0), 10 mM europium(II) 1,4,7,10-tetrakis(carbamoylmethyl)-1,4,7,10-tetraazacyclododecane (Eu^{II}-DOTAM; $E_{1/2}$ = –0.59 V at pH 8.0), 10 mM europium(II) 1,4,7,10-tetraazacyclododecane-1,4,7,10-tetraacetic acid (Eu^{II}-DOTA; $E_{1/2}$ = –0.92 V at pH 8.0), and 10 mM europium(II) diethylenetriamine pentaacetate (Eu^{II}-DTPA; $E_{1/2}$ = –1.14 V at pH 8.0), and monitored the intensity of the all-ferrous, g = 16.4 parallel-mode EPR signal at the various reduction potentials created by these reductants (Figure 5b).[16,37] In the case of *Av*NifH, the g = 16.4 signal are absent from the EPR spectra at –0.44 V (*i.e.*, 20 mM dithionite) and –0.47 V (*i.e.*, 2 mM dithionite); whereas in the case of *Av*NifH^{Se}, the intensities of the g = 16.4 signal are 4% and 13%, respectively, of the maximum intensity at –0.44 V and –0.47 V. Plotting of the intensity of the g = 16.4 signal *versus* the reductant potentials allowed for an approximate assignment of the 'mid-intensity' potential, or the potential corresponding to 50% of the maximum signal intensity, for *Av*NifH and *Av*NifH^{Se} (Figure 5c). Strikingly, the 'mid-intensity' potential for *Av*NifH is ~–0.90 V, which approximates the midpoint potential of –0.79 V previously determined for the $[Fe_4S_4]^{1+/0}$ couple by a redox mediator-based method.[38] Based on this observation, the 'mid-intensity' potential for *Av*NifH^{Se}, which is ~–0.59 V, may very well represent the approximate midpoint potential of the $[Fe_4Se_4]^{'1+'/0}$ couple. Thus, like the $[Fe_4Se_4]^{2+/'1+'}$ couple, the $[Fe_4Se_4]^{'1+'/0}$ couple likely has a more positive midpoint potential than its $[Fe_4S_4]$ counterpart, which could in turn impact the reactivity of *Av*NifH in catalysis and assembly.

Indeed, while both *Av*NifH and *Av*NifH^{Se} can reduce CO_2 to CO under ambient conditions in the presence of Eu^{II}-DTPA (Figure 6a), *Av*NifH^{Se} shows reduced activity in this reaction compared to *Av*NifH, consistent with a more positive reduction potential (or a weaker reducing power) of the Eu^{II}-DTPA reduced, all-ferrous cluster in the former protein than its counterpart in the latter protein. In the presence of 20 mM dithionite, however, no CO can be detected as a product of CO_2 reduction by *Av*NifH; whereas *Av*NifH^{Se} can reduce CO_2 to CO in the same reaction at 15% in of the maximum yield achieved in the presence of Eu^{II}-DTPA (Figure 6a). Given the partial all-ferrous feature of the $[Fe_4Se_4]^{'1+'}$ cluster and the absence of this feature from the $[Fe_4S_4]^{1+}$ cluster, this observation implies the necessity

to have the cluster of *Av*NifH poised in the all-ferrous state to enable CO_2 reduction, a condition suggested by our previous DFT calculations of this reaction.[9]

The difference in the reactivities of *Av*NifH and *Av*NifH^{Se} is further illustrated by the difference in the activities achieved by pairing these proteins with their respective partners in substrate reduction (Figure 6b) and cluster maturation (Figure 6c and 6d). Combined with *Av*NifDK, *Av*NifH^{Se} shows only 20.5%, 18.5% and 17.4%, respectively, of the activities achieved by *Av*NifH in N_2-, C_2H_2- and H^+-reduction based on the total electron fluxes in these reactions (Figure 6b). Similarly, when paired with *Av*NifEN, *Av*NifH^{Se} shows a reduced activity at 83% relative to that of *Av*NifH in maturing the cofactor precursor ([Fe_8S_9C]) into a fully complemented M-cluster ([(*R*-homocitrate)$MoFe_7S_9C$]) (Figure 6c); yet, when partnered with the *Av*NifDK variant containing the P-cluster precursor (designated *Av*NifDK^{P}*), *Av*NifH^{Se} demonstrates a nearly unchanged activity at 99% of that of *Av*NifH in converting the P-cluster precursor (a [Fe_4S_4] pair, designated the P*-cluster) into a mature P-cluster ([Fe_8S_7]) (Figure 6d).

The disparate abilities of *Av*NifH and *Av*NifH^{Se} to enable substrate reduction and cluster maturation could result from differential redox properties of the clusters within the two Fe proteins and/or from differential interactions of the two Fe proteins with their partners in these reactions. To discern between the two possible causes for the differential activities of *Av*NifH and *Av*NifH^{Se}, we measured chelation of the cluster Fe atoms of *Av*NifH and *Av*NifH^{Se} with an Fe chelator, bathophenanthroline, in the presence of *Av*NifDK, *Av*NifDK^{P}* and *Av*NifEN by UV/Vis spectroscopy and compared the levels at which the cluster Fe atoms in *Av*NifH and *Av*NifH^{Se} were protected from chelation upon docking of these Fe proteins onto their respective partner proteins in substrate reduction and cluster maturation. Interestingly, compared to *Av*NifH, *Av*NifH^{Se} is protected from Fe chelation at 97%, 93% and 73%, respectively, in the presence of *Av*NifDK, *Av*NifDK^{P}* and *Av*NifEN (Figure 6e). Using the protection level of Fe chelation as a measure for protein-protein interaction between the Fe protein and its partner protein, *Av*NifH^{Se} is indistinguishable from *Av*NifH in its interaction with *Av*NifDK (Figure 6e); yet, it has significantly decreased substrate reduction activities than *Av*NifH (Figure 6b), suggesting that the difference in the redox properties of the two Fe proteins is likely the underlying reason for the discrepancy in their catalytic capabilities. In contrast, the interactions of *Av*NifH^{Se} with *Av*NifDK^{P}* and *Av*NifEN, respectively, in P- and M-cluster maturation, as compared to those of *Av*NifH with the same proteins in these processes (Figure 6e), align well with the percentage maturation activities of *Av*NifH^{Se} relative to *Av*NifH in these reactions (Figure 6c, d), pointing to an impact of differential protein-protein interactions—rather than differential redox properties of the two Fe proteins—on cluster maturation. This observation is important, as it implies a difference in the redox requirement for the Fe protein in catalysis and assembly. It is likely that the catalytic events necessitate a lower reduction potential than the cluster assembly processes, hence the substantially reduced activities in catalysis, yet unimpacted activities in assembly, upon substitution of Se for S and increase of the reduction potential of the cluster in *Av*NifH.

Conclusion

In this work, we synthesized a water-soluble [Fe_4Se_4] cluster that allowed for a 'clean' reconstitution of the apo *Av*NifH protein with the Se-substituted cluster. Our biochemical, EPR and XAS/EXAFS analyses demonstrated the ability of the [Fe_4Se_4] cluster to adopt the super-reduced, all-ferrous state, a feat that cannot be directly achieved via chemical synthesis, upon incorporation of this cluster into *Av*NifH. Moreover, these studies revealed a more positive reduction potential of the [Fe_4Se_4] cluster than its [Fe_4S_4] counterpart in *Av*NifH, which could be used to distinguish the differential redox requirements for the functions of *Av*NifH in catalysis and assembly. Variation of the reductase component of nitrogenase (*i.e.*, the Fe protein),[39,40] along with site-directed mutagenesis of the active site environment and alteration of the heterometal or organic moiety of the cofactor in this enzyme,[41–44] has proven effective in accumulating catalytic intermediates for mechanistic studies of nitrogenase. The utility of the approach that selectively substitutes the bridging sulfides of FeS clusters with selenides, as demonstrated in the previous work on *Kp*NifH[20] and in the current study on *Av*NifH, can be further expanded to facilitate mechanistic studies of both catalysis and biosynthesis of nitrogenase. Specifically, the bridging sulfides of the FeS clusters in *Av*NifDK and *Av*NifEN, the catalytic or assembly partners of the Fe protein, can be replaced by Se or other chalcogens, such as Te, to alter the redox and/or structural properties of the FeS clusters in these proteins. These Se/Te-substituted forms of *Av*NifDK and *Av*NifEN can then be strategically combined with the S-containing or Se/Te-substituted *Av*NifH to capture catalytically or biosynthetically relevant intermediates for further characterization by biochemical, spectroscopic and structural approaches. The outcome of the current study provides an important framework for future mechanistic studies of nitrogenase along this line, with an ultimate goal to decipher the intricate catalytic and biosynthetic processes of this unique metalloenzyme.

Supplementary Material

Refer to Web version on PubMed Central for supplementary material.

Acknowledgements

This work was supported by NSF CAREER grant CHE-1651398 (Y.H.) and NIH-NIGMS grant GM67626 (M.W.R., Y.H.). XAS data were collected at Beamlines 7–3 and 9–3 at the Stanford Synchrotron Radiation Lightsource, SLAC National Accelerator Laboratory. Stanford Synchrotron Radiation Lightsource operations is supported by the U.S. Department of Energy, Office of Science, Office of Basic Energy Sciences under Contract No. DE-AC02-76SF00515. The SSRL Structural Molecular Biology Program is supported by the DOE Office of Biological and Environmental Research, and by the National Institutes of Health, National Institute of General Medical Sciences (P30GM133894) (K.H.).

References

[1]. Rees DC, Annu. Rev. Biochem 2002, 71, 221–246. [PubMed: 12045096]

[2]. Burgess BK, Lowe DJ, Chem. Rev 1996, 96, 2983–3012. [PubMed: 11848849]

[3]. Buscagan TM, Rees DC, Joule 2019, 3, 2662–2678. [PubMed: 32864580]

[4]. Rutledge HL, Tezcan FA, Chem. Rev 2020, 120, 5158–5193. [PubMed: 31999100]

[5]. Jasniewski AJ, Lee CC, Ribbe MW, Hu Y, Chem. Rev 2020, 120, 5107–5157. [PubMed: 32129988]

[6]. Schindelin H, Kisker C, Schlessman JL, Howard JB, Rees DC, Nature 1997, 387, 370–376. [PubMed: 9163420]

[7]. Tezcan FA, Kaiser JT, Mustafi D, Walton MY, Howard JB, Rees DC, Science 2005, 309, 1377–1380. [PubMed: 16123301]

[8]. Rebelein JG, Stiebritz MT, Lee CC, Hu YY, Nat. Chem. Biol 2017, 147–149. [PubMed: 27893704]

[9]. Stiebritz MT, Hiller CJ, Sickerman NS, Lee CC, Tanifuji K, Ohki Y, Hu Y, Nat. Catal 2018, 1, 444–451.

[10]. Lee CC, Stiebritz MT, Hu Y, Acc. Chem. Res 2019, 1168–1176. [PubMed: 30977994]

[11]. Hu YY, Ribbe MW, Angew. Chem. Int. Ed. Engl 2016, 55, 8216–8226. [PubMed: 27206025]

[12]. Lee CC, Hu Y, Ribbe MW, Angew. Chem. Int. Ed. Engl 2011, 50, 5545–5547. [PubMed: 21538750]

[13]. Hu Y, Lee CC, Ribbe MW, Science 2011, 333, 753–755. [PubMed: 21817053]

[14]. Hu Y, Ribbe MW, Annu. Rev. Biochem 2016, 85, 455–483. [PubMed: 26844394]

[15]. Ribbe MW, Hu Y, Hodgson KO, Hedman B, Chem. Rev 2014, 114, 4063–4080. [PubMed: 24328215]

[16]. Angove HC, Yoo SJ, Menck E, Burgess BK, J. Biol. Chem 1998, 273, 26330–26337. [PubMed: 9756863]

[17]. Vincent KA, Tilley GJ, Quammie NC, Streeter I, Burgess BK, Cheesman MR, Armstrong FA, Chem. Commun 2003, 2590–2591.

[18]. Rettberg LA, Stiebritz MT, Kang W, Lee CC, Ribbe MW, Hu Y, Chemistry 2019, 25, 13078–13082. [PubMed: 31402524]

[19]. Zheng L, White RH, Cash VL, Dean DR, Biochemistry 1994, 33, 4714–4720. [PubMed: 8161529]

[20]. Hallenbeck PC, George GN, Prince RC, Thorneley RN, J. Biol. Inorg. Chem 2009, 14, 673–682. [PubMed: 19234722]

[21]. The structural data is available from the Cambridge Crystallographic Data Centre at https://www.ccdc.cam.ac.uk/structures/ with the CCDC depository number 2121572.

[22]. Bonomi F, Werth MT, Kurtz DM Jr., Inorg. Chem 1985, 24, 4331–4335

[23]. Kern A, Näther C, Studt F, Tuczek F, Inorg. Chem 2004, 43, 5003–5010. [PubMed: 15285677]

[24]. Yu SB, Papaefthymiou GC, Holm RH, Inorg. Chem 1991, 30, 3476–3485.

[25]. Bobrik MA, Laskowski EJ, Johnson RW, Gillum WO, Berg JM, Hodgson KO, Holm RH, Inorg. Chem 1978, 17, 1402–1410.

[26]. Carney MJ, Papaefthymiou GC, Whitener MA, Spartalian K, Frankel RB, Holm RH, Inorg. Chem 1988, 27, 346–352.

[27]. Ciurli S, Yu SB, Holm RH, Srivastava KKP, Münck E, J. Am. Chem. Soc 1990, 112, 8169–8171.

[28]. Hauptmann R, Schneider J, Chen C, Henkel G, Acta Cryst. C 1999, 55, 192–194.

[29]. Barclay JE, Davies SC, Evans DJ, Hughes DL, Longhurst S, S. Inorg. Chim. Acta 1999, 291, 101–108.

[30]. Tan LL, Holm RH, Lee SC, Polyhedron 2013, 58, 206–217. [PubMed: 24072952]

[31]. Yang L, Powell DR, Houser RP, Dalton Trans 2007, 955–964. [PubMed: 17308676]

[32]. Okuniewski A, Rosiak D, Chojnacki J, Becker B, Polyhedron 2015, 90, 47–57.

[33]. Westre TE, Kennepohl P, DeWitt JG, Hedman B, Hodgson KO, Solomon EI, J. Am. Chem. Soc 1997, 119, 6297.

[34]. Sarangi R, Coord. Chem. Rev 2013, 257, 459–472. [PubMed: 23525635]

[35]. Moulis JM, Auric P, Gaillard J, Meyer J, J. Biol. Chem 1984, 259, 11396–11402 [PubMed: 6088543]

[36]. Gaillard J, Moulis JM, Auric P, Meyer J, Biochemistry 1986, 25, 464–468. [PubMed: 3955006]

[37]. Solomon JB, Rasekh MF, Hiller CJ, Lee CC, Tanifuji K, Ribbe MW, Hu Y, JACS Au 2020, 1, 119–123. [PubMed: 34467276]

[38]. Guo M, Sulc F, Ribbe MW, Farmer PJ, Burgess BK, J. Am. Chem. Soc 2002, 124, 12100–12101. [PubMed: 12371842]

[39]. Hiller CJ, Stiebritz MT, Lee CC, Liedtke J, Hu Y, Chemistry 2017, 23, 16152–16156. [PubMed: 28984391]

[40]. Lee CC, Wilcoxen J, Hiller CJ, Britt RD, Hu Y, Angew. Chem. Int. Ed. Engl 2018, 57, 3411–3414. [PubMed: 29409145]

[41]. Lee CC, Tanifuji K, Newcomb M, Liedtke J, Hu Y, Ribbe MW, Chembiochem 2018, 19, 649–653. [PubMed: 29363247]

[42]. Rebelein JG, Lee CC, Newcomb M, Hu Y, Ribbe MW, mBio 2018, 9, e00310–18. [PubMed: 29535200]

[43]. Newcomb MP, Lee CC, Tanifuji K, Jasniewski AJ, Liedtke J, Ribbe MW, Hu Y, Chembiochem 2020, 21, 1742–1748. [PubMed: 31747483]

[44]. Liedtke J, Lee CC, Tanifuji K, Jasniewski AJ, Ribbe MW, Hu Y, Chembiochem 2021, 22, 151–155. [PubMed: 32918851]

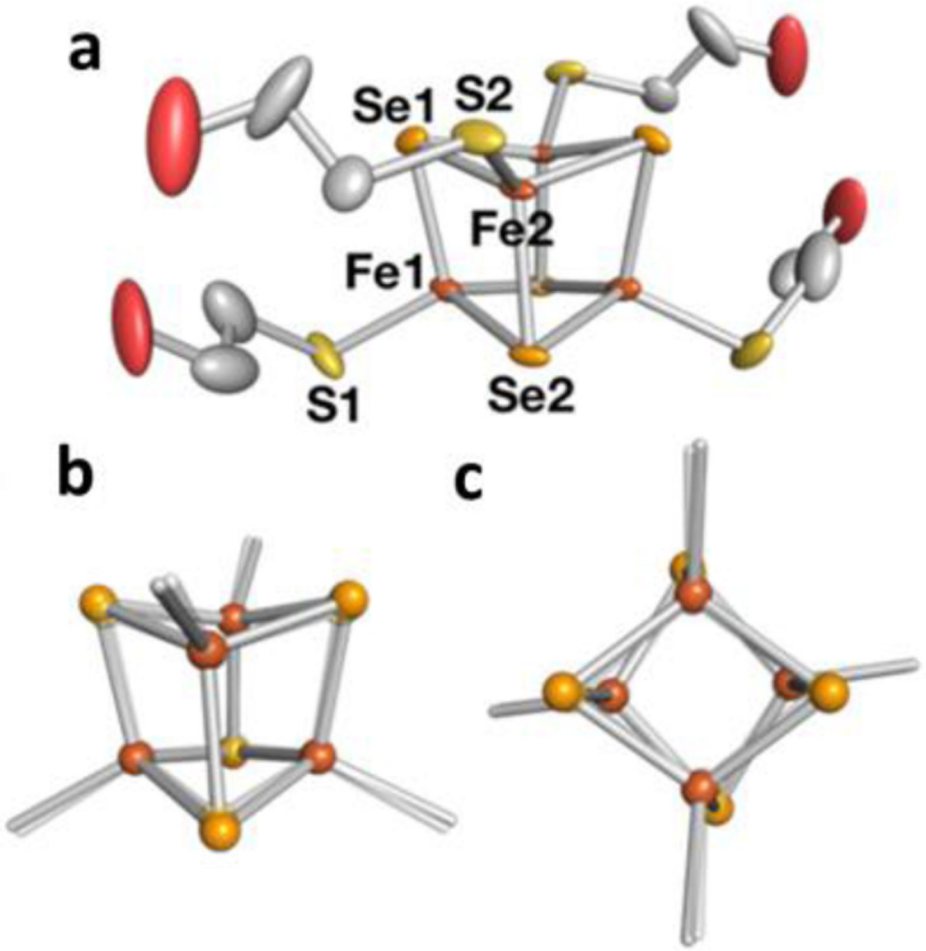

Figure 1.

Structure of $[Fe_4Se_4]^{Syn}$. (a) Crystal structure of $[Fe_4S_4]^{Syn}$, with the thermal ellipsoids set at a probability level of 50%. (b, c) Overlay of the core structures of $[Fe_4Se_4]^{Syn}$ (solid) and $[Fe_4S_4]^{Syn}$ (transparent) in side (b) and top (c) views. $[Fe_4Se_4]^{Syn}$, $[PPh_4]_2[Fe_4Se_4(SCH_2CH_2OH)_4]$; $[Fe_4S_4]^{Syn}$, $[PPh_4]_2[Fe_4S_4(SCH_2CH_2OH)_4]$. The $[PPh_4]$ cations and hydrogen atoms are omitted from the structures for purpose of clarity.

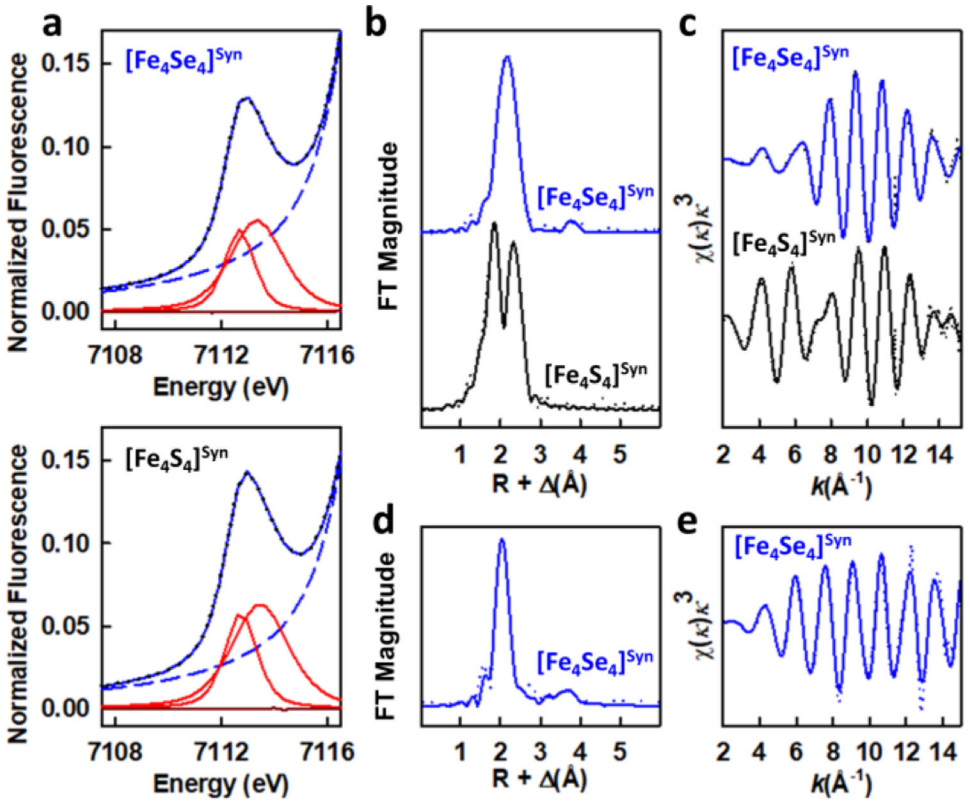

Figure 2.

Fe and Se K-edge XAS/EXAFS analyses of $[Fe_4Se_4]^{Syn}$. (a) Pre-edge region analysis of $[Fe_4Se_4]^{Syn}$ (upper) and $[Fe_4S_4]^{Syn}$ (lower). Shown are the experimental data (black dotted), the baseline (red dashed), the pre-edge peak components (red solid), the residuals (brown solid) and the total fit (blue solid). Fe (b, c) and Se (d, e) K-edge EXAFS data (dotted) and best fits (solid) of $[Fe_4Se_4]^{Syn}$ (blue) and $[Fe_4S_4]^{Syn}$ (black). Shown are the Fourier transformed EXAFS data (b, d) and the k^3-weighted EXAFS data (c, e). See Supporting Information (Tables S5–S9) for details of fits.

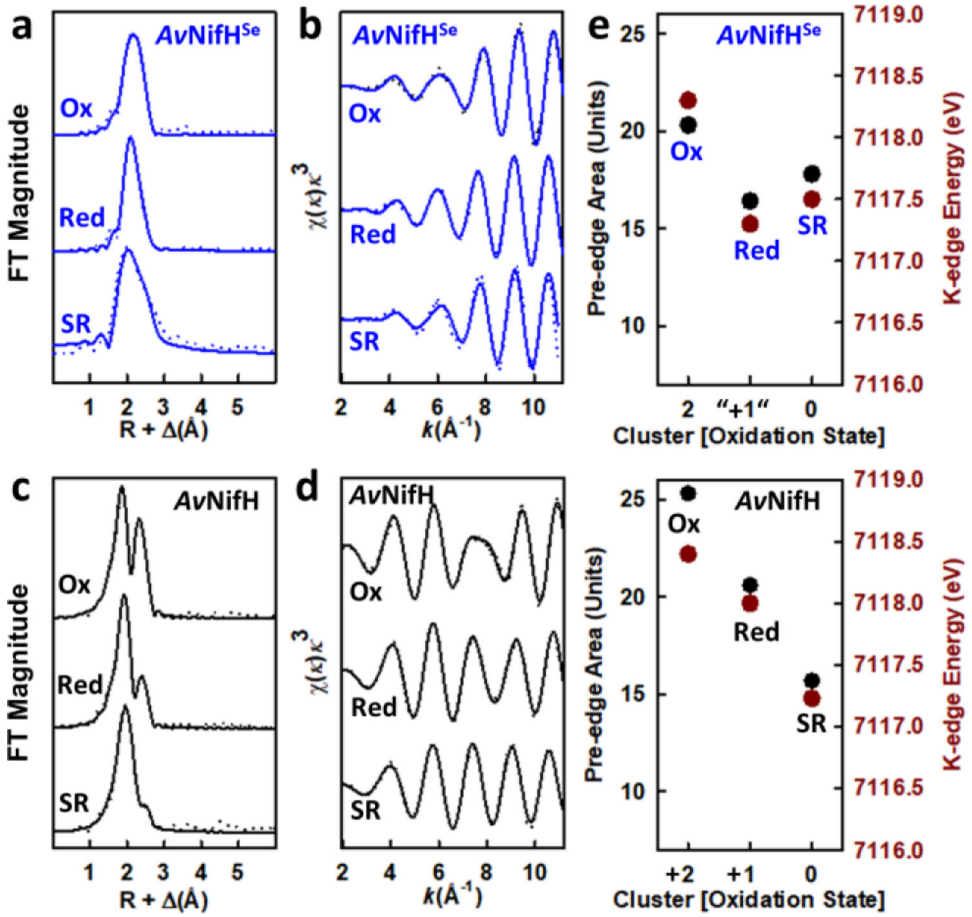

Figure 3.

Fe K-edge XAS/EXAFS analysis of *Av*NifH^{Se}. Fe K-edge EXAFS data (dotted) and best fits (solid) of *Av*NifH^{Se} (a, b) and *Av*NifH (c, d) in the oxidized, reduced, and super-reduced states. Shown are the Fourier transformed EXAFS data (a, c) and the k^3-weighted EXAFS data (b, d). See Supporting Information (Tables S5, S6, S10–S15) for details of fits. (e) Pre-edge area (black) and Fe K-edge energy (brown) of *Av*NifH^{Se} (upper) and *Av*NifH (lower) *versus* oxidation state. The oxidized (Ox), reduced in (Red) and super-reduced (SR) states were generated by treating *Av*NifH^{Se} or *Av*NifH with IDS, dithionite and Eu^{II}-DTPA (or Ti^{III} citrate), respectively.

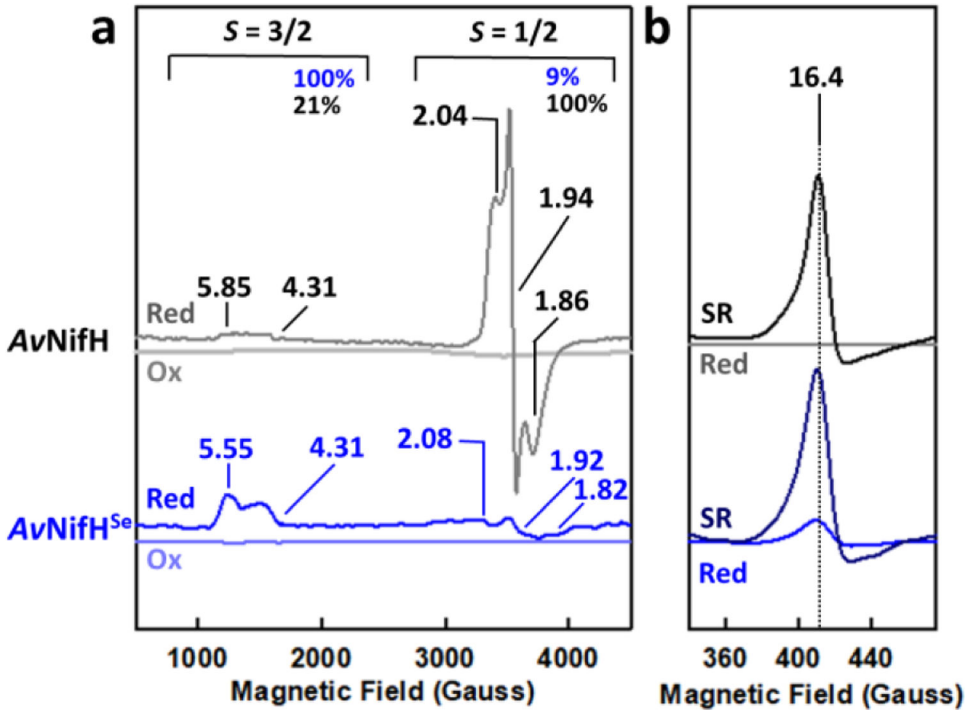

Figure 4.

EPR analysis of *Av*NifH^{Se}. Shown are the perpendicular-mode (a) and parallel-mode (b) EPR spectra of *Av*NifH^{Se} and *Av*NifH in the oxidized (Ox), reduced (Red) and super-reduced (SR) states. The g values of the $S = 1/2$ and $S = 3/2$ signals in the reduced state are indicated (a), along with the $g = 16.4$ signal that is characteristic of the super-reduced, all-ferrous state (b).

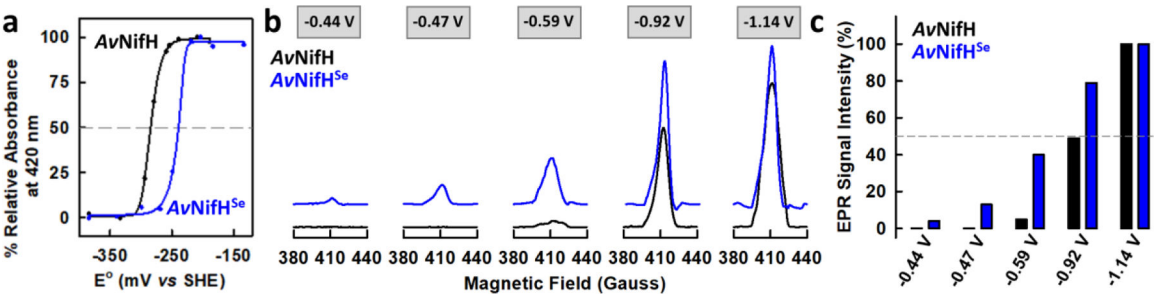

Figure 5.

Redox properties of *Av*NifH^{Se}. (a) Determination of the midpoint potentials of $[Fe_4Se_4]^{'1+'/2+}$ in *Av*NifH^{Se} (blue) and $[Fe_4Se_4]^{1+/2+}$ in *Av*NifH (black) using the following redox mediator dyes: methyl viologen, benzyl viologen, safranin O, and phenosafranin. (b) Appearance of the all-ferrous-specific, $g = 16.4$ parallel-mode EPR signals upon treatment of *Av*NifH^{Se} (blue) or *Av*NifH (black) with various reductants. (c) The intensity of the $g = 16.4$ signal of *Av*NifH^{Se} (blue) or *Av*NifH (black) *versus* the potential of the reductant used to generate the signal. The EPR signal intensity (%) was determined by double integration of the $g = 16.4$ signal and calculation of the relative intensity *versus* the maximum intensity at –1.14 V. The 'mid-intensity' potential, or the potential corresponding to 50% of the maximum signal intensity, is indicated by a horizontal dashed line.

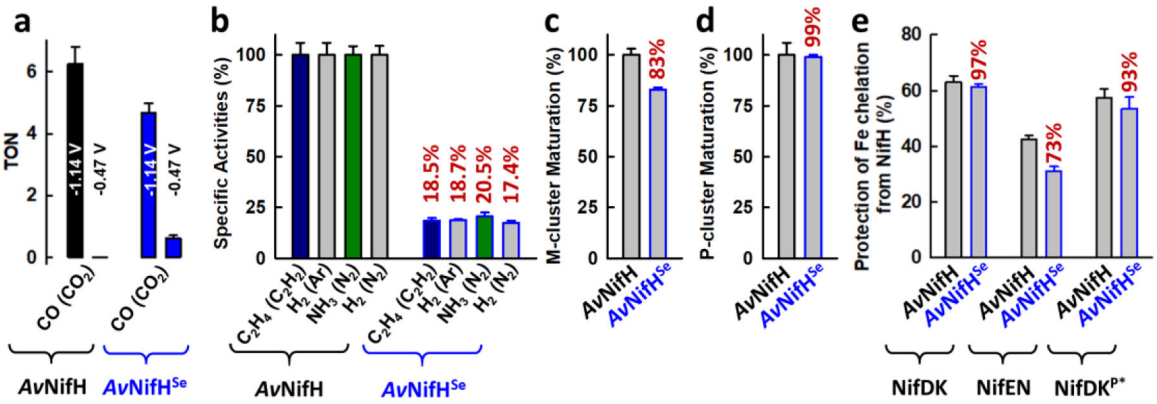

Figure 6.

Catalytic and biosynthetic activities of *Av*NifH^{Se}. (a) Reduction of CO_2 to CO by *Av*NifH^{Se} (blue) or *Av*NifH (black) as an independent reductase. (b) Reduction of C_2H_2, H^+ (under Ar) and N_2 to C_2H_4, H_2 and NH_3/H_2, respectively, with *Av*NifH^{Se} (blue) or *Av*NifH (black) serving as the reductase component for the catalytic component, *Av*NifDK, within the nitrogenase complex. (c) Maturation of the P-cluster, with *Av*NifH^{Se} or *Av*NifH reductively couples a $[Fe_4S_4]$ cluster pair (precursor) into a $[Fe_8S_7]$ cluster (P-cluster) at the α/β interface of *Av*NifDK^{P}*. (d) Maturation of the M-cluster, with *Av*NifH^{Se} or *Av*NifH serving as a Mo/homocitrate insertase for the maturation of a $[Fe_8S_9C]$ cluster (precursor) into an [(*R*-homocitrate)$MoFe_7S_9C$] cluster (M-cluster) on the assembly scaffold protein, *Av*NifEN, prior to transfer of the M-cluster from *Av*NifEN to the cofactor binding site of apo *Av*NifDK. (e) Protection of the cluster Fe atoms of *Av*NifH^{Se} or *Av*NifH from chelation upon interaction with *Av*NifDK, *Av*NifDK^{P}* and *Av*NifEN, respectively, in substrate reduction (*see* b) and P- and M-cluster maturation (*see* c and d). Eu^{II}-DTPA (a) and dithionite (b-d) were used as reductants, without (a) or with (b-d) ATP, in these *in vitro* activity assays.